Fault Detection Methods for Three-Level NPC Inverter Based on DC-Bus Electromagnetic Signatures

Ibtissem Abari, Ali Lahouar, Mahmoud Hamouda, *Member, IEEE*, Jaleleddine Ben Hadj Slama, *Senior Member, IEEE*, and Kamal Al-Haddad, *Fellow, IEEE*

***Abstract*—This paper proposes two new open-circuit fault detection methods suitable for the diagnosis of power electronics converters. The faulty semiconductor devices are identified using conducted and radiated electromagnetic signatures of the dc bus through nonintrusive measurements. The first method uses a low-cost electromagnetic interference filter to collect the common-mode emissions signature. The second one utilizes an external antenna to collect the emitted near-field signature. Both methods are tested on a three-level neutral point clamped inverter (NPC) inverter with the aim to identify the clamping diodes open-circuit faults. Indeed, each open-circuit fault affects the common-mode emission signature in the time-domain, while the fast Fourier transform of the emitted near-field showed substantial reduction of spectrum amplitude at a specific radio frequency range and the appearance of a new spectral rail. The effectiveness of these two methods has been tested through numerical simulations and validated by experimental results which confirmed its high performance in detecting single as well as multiple open-circuit faults for three-level NPC inverter.**

***Index Terms*—Converter's reliability, electromagnetic interference (EMI) filter, electromagnetic signature, fault diagnosis, multilevel converter, near-field, neutral point clamped inverter (NPC) converter, open-circuit fault.**

I. Introduction

IN RECENT years, multilevel converters have received a remarkable interest and have been widely studied especially for medium-voltage and high power industrial applications [1]–[3]. The three-level neutral point clamped inverter (NPC) is one of the most promising topologies that has been introduced on the commercial market several years ago. Nowadays, the latter is widely used in many industrial processes, such as motor drives, grid-connected renewable resources interface, etc. [4]. However, the large number of switching devices involved increased the failure probability of the converter as compared, for example, with the conventional two-level inverter. This concern has therefore stimulated the research effort toward the development of accurate and fast identification techniques to identify the faulty power semiconductors with the aim to prevent fault propagation and hence limiting the resulting failure cost [5].

Power semiconductor devices failure can be classified into two categories: short-circuit and open-circuit faults [6]. A short-circuit fault may have some inherently undesirable impacts on the system due to excessive current flowing through the affected device and associated path. Therefore, an immediate shutdown of the inverter is required to guarantee limited damage. On the other hand, the open-circuit faults are not likely to cause serious damage compared to the short-circuit ones. Still, they lead to some secondary disturbances in the remaining part of the converter [7].

Though the methods proposed in this paper are based on new nonintrusive diagnosis techniques, the state of the art of the conventional intrusive fault detection methods is hereafter presented with the aim to discuss their performance.

Most of the conventional intrusive diagnosis techniques applied to detect open-circuit faults in NPC inverters are based on current or/and voltage signature analysis methods. In [8], Lee *et al*. proposed an open-circuit fault detection method for grid tie NPC inverter based on grid current distortion analysis. However, injection of reactive current is needed in order to identify the faulty switch. In [9], the fault detection method is based on the comparison of the dimension of the Concordia current pattern with the healthy case. The main drawback of this method is the need of one additional fundamental load cycle to estimate the current pattern angle for the identification of the faulty switch. In [10], the average current Park's vector is used to perform the identification of a single faulty IGBT. However, the identification algorithm needs the analysis of three additional variables to be diagnosed. In [11], the slope method, based on the analysis of the phase current distortion is proposed with the aim to identify the faulty switches of a back-to-back NPC converter. This method is able to detect the faulty switch in the rectifier

Manuscript received March 13, 2017; revised June 7, 2017, August 9, 2017, and September 21, 2017; accepted October 9, 2017. Date of publication November 24, 2017; date of current version March 6, 2018. *(Corresponding author: Kamal Al-Haddad.)*

I. Abari, A. Lahouar, M. Hamouda, and J. B. H. Slama are with the Research Laboratory LATIS, National Engineering School of Sousse, University of Sousse, Technopole of Sousse, Sousse 2054, Tunisia (e-mail: ibtissem_abari@yahoo.fr; ali.lahouar@gmail.com; mahmoudhamouda@yahoo.fr; bhslama@yahoo.fr).

K. Al-Haddad is with the Ecole de Technologie Superieure, University of Quebec, Montreal, QC H3C1K3, Canada (e-mail: kamal.al-haddad@etsmtl.ca).

Color versions of one or more of the figures in this paper are available online at http://ieeexplore.ieee.org.

Digital Object Identifier 10.1109/TIE.2017.2777378

stage. However, for the inverter stage, the identification of the faulty device among the two upper or two lower switches remains impossible. In [12], Farnesi *et al*. used a Rogowski coil in series with each clamping diode and three current sensors to identify the faulty transistors of the NPC inverter. For each leg, the detection of the open-circuit fault of switches needs the knowledge of the currents in the clamping diodes, along with the phase current. The main drawbacks of this method are the need of six additional Rogowski type of coils, and also accurate knowledge of the instantaneous devices switching states to identify the outer transistors fault. Nonetheless, one common remaining problem of current-based identification methods is their sensitivity to low-frequency disturbances, which affect the currents waveforms and may cause false detection alarms. Methods relying on currents' signature, are also supposed to become ambiguous for small values of load currents [13].

A diagnosis method based on measurement of the modulated pole voltages duration times was proposed in [14]. Several diagnosis methods have also been developed based on the analysis of both ac currents and modulated pole voltages signatures. In [15], the inverter's output voltage and load current are used to perform a real-time identification of single and multiple open-circuit faults in each power device within one modulation period. In [16], a detection method of faulty power switch or faulty clamping diode based on the analysis of both output currents and voltage waveforms was proposed. This method allowed the exact identification of the faulty power switch or/and the clamping diode through a modified control algorithm. Notice that most diagnosis methods based on the analysis of the modulated output voltages are costly due to the extra wide bandwidth voltage sensors needed. Moreover, they require prior knowledge of power devices' switching states. This implies that the diagnosis algorithm requires data from the modulation algorithm.

The conventional intrusive diagnosis methods have been likewise applied to diagnose other multilevel topologies mainly the modular multilevel converters (MMC). In [17], the modulated output voltages are utilized to diagnosis open-circuit faults in MMC by applying the support vector machine method. In [18], a diagnosis method based on the frequency analysis of output voltage has been proposed. This method is able to identify only the faulty cell of the MMC. In [19], a state observer of the current circulating through the upper and lower arms and the load current is constructed with the aim to identify the faulty arm. Thereafter, the faulty submodule (SM) of the specified arm is identified based on its capacitor voltage value; the latter increases as compared to the healthy case operation. This method is able to identify the faulty switch only in half-bridge (SM) and has not been extended to the case of H-bridge (SM). In [3], a diagnosis method based on the monitoring of the load current and phase-to-neutral output voltage has been proposed for cascaded H-bridge multilevel inverter. This method allows the identification of the faulty active switch and permits to isolate the faulty cell. However, it needs prior knowledge of the switch state, implying therefore that the diagnosis algorithm needs data from the modulation algorithm.

On the other hand, few nonintrusive diagnosis methods were recently proposed for open-circuit fault diagnosis of two-level

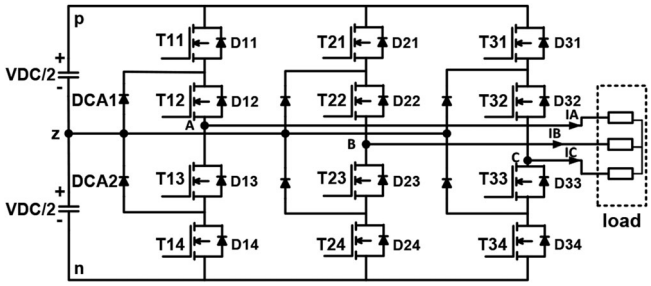

Fig. 1. Three-level NPC inverter power circuit.

inverters and dc/dc converters. In [20], an open-circuit fault is detected, based on the harmonic spectrum of the stray magnetic and electric fields provided by a two-level inverter. This method is nonintrusive and it does not need any additional sensor. However, it is limited to the low-frequency band and it cannot locate the exact faulty switch. In [21], a monitoring and diagnosis method based on the magnetic near-field measurement is proposed to detect the open-circuit faults of dc–dc converter. The major restriction of this method can be generalized in its disability to identify the exact faulty switch of the full bridge converter.

In this paper, two pioneering methods for the detection of open-circuit faults in power converters are proposed. The first method uses the dc-bus conducted emissions signature measured across an electromagnetic interference (EMI) filter. The second method is based on the frequency spectrum signature of the near-field emitted above the converter's dc bus. The proposed two methods need only the use of one of the following nonintrusive sensors. A simple EMI filter connected between the inverter dc-terminal and the dc source, or a near-field antenna placed above the dc-bus cable. It is shown that the gathered information from these sensors is sufficient to detect the clamping diodes open-circuit faults in a three-level NPC inverter. Notice that clamping diodes open-circuit faults are chosen as a case study to validate this new approach. Diodes failures are, certainly, not the only recurrent fault in power electronic systems [22]. Clamping diodes are however chosen in this paper because they are fault-tolerant. Therefore, the correct identification of a faulty clamping diode will allow the use of a fault-tolerant algorithm and avoid an immediate shutdown of the NPC inverter.

Compared to conventional intrusive techniques, the proposed nonintrusive methods are not sensitive to low-frequency disturbances since the diagnosis is based on high-frequency EMI signatures. Moreover, only one extra voltage sensor is needed compared to three extra sensors required by the output voltages signatures-based diagnosis techniques. Notice also that the near-field-based diagnosis sensor (antenna) is completely decoupled from the electrical circuit. Therefore, any fault on the power circuit would not have the chance to propagate into the diagnosis circuit.

The remainder of this paper is organized as follows. Section II describes the functional bloc diagram and the operation standards of the three-level NPC inverter. It also provides an inclusive explanation of the clamping diode open-circuit fault

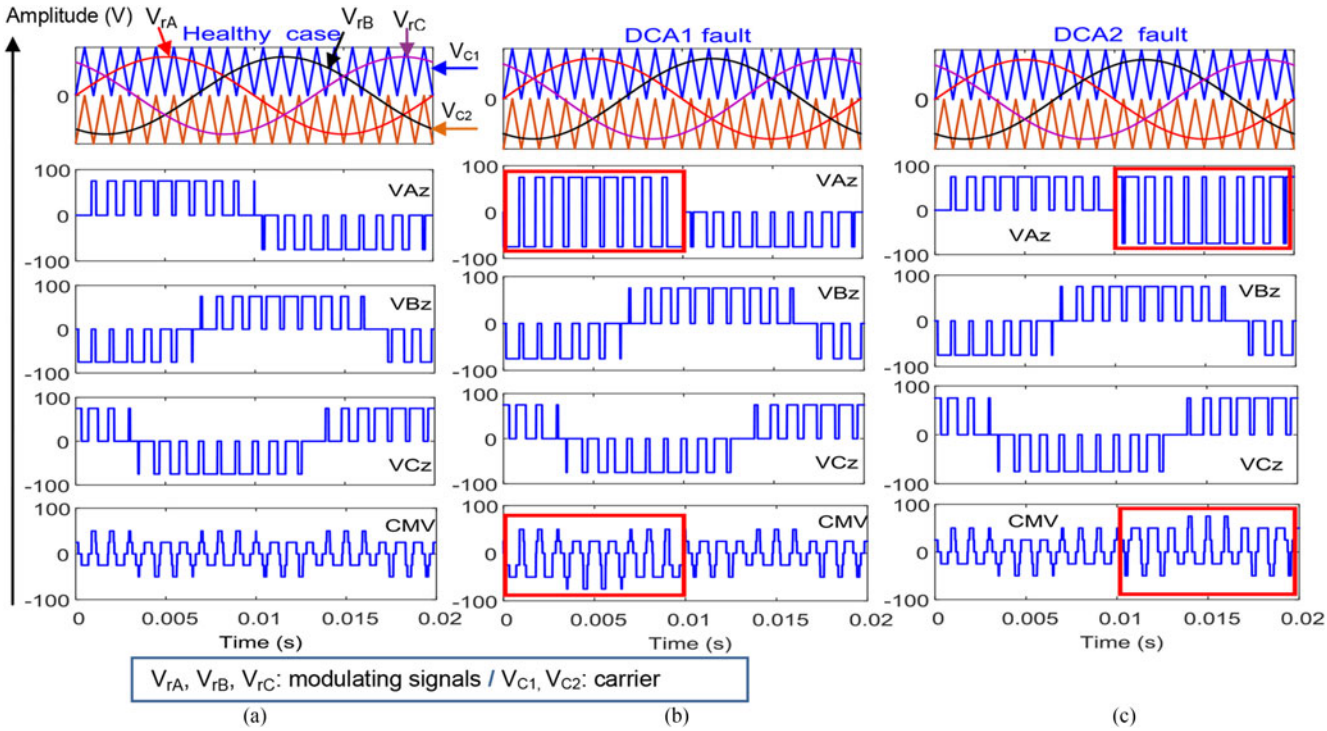

Fig. 2. Typical waveforms of the pole voltages (V_{Az}, V_{Bz}, and V_{Cz}) and common-mode voltage CMV obtained in (a) healthy condition, (b) DCA1 fault, and (c) DCA2 fault.

effect on the output voltages and currents along with a theoretical analysis. Section III discusses the numerical simulations based on a high-frequency model of the converter. Experimental results and fault detection methods based on the conducted emissions and near-field signatures are presented in Sections IV and V, respectively. Finally, general remarks and conclusions are provided in Section VI.

II. NPC Inverter Operation Under Open-Circuit Clamping Diode Fault

A. NPC Inverter Operation in Healthy Condition

The schematic bloc diagram of the three-level NPC inverter is illustrated in Fig. 1. Each inverter leg consists of four power switches connected in series and of two clamping diodes connected to the midpoint z of the dc-bus capacitors. The inverter is fed by a dc voltage source through two series-connected electrolytic capacitors. For each leg, three switching states are possible, namely P (positive), O (zero), and N (negative). These states provide a three-level pole voltage referred to the midpoint z. The three voltage levels are $-VDC/2$, 0, and $+VDC/2$, respectively. Several modulation algorithms can be applied to synthesize the required target output voltages V_{Az}, V_{Bz}, and V_{Cz}. Though the space vector modulation technique provides better performance than the multicarrier sinusoidal pulse width modulation method in terms of current THD, the latter is adopted in this paper because of its digital implementation simplicity. Knowing the operation mode of the three-level NPC inverter, each clamping diode operates when the switching state O is activated. DCA1 is able to conduct during the positive half-cycle of the phase current, whereas DCA2 conducts during the negative half-wave of the same phase current.

As an example, for a time interval equal to the half-period of the output voltage fundamental cycle, that is to say for a 50 Hz output signal, the clamping diodes are solicited during 10 ms only. Typical waveforms of the pole voltages and common mode voltage (CMV) under normal operation conditions are shown in Fig. 2(a).

The CMV is computed as follows:

$$\mathrm{CMV} = V_{gz} = \frac{V_{Az} + V_{Bz} + V_{Cz}}{3}. \tag{1}$$

Therefore, the diode DCA1 is able to conduct the load current during the time interval [0, 10] ms; while the diode DCA2 conduction occurs during the second half-period [10, 20] ms. The same explanation is valid for the other two remaining legs of the inverter, considering a phase shift of 2 π/3.

B. NPC Inverter Operation Under Faulty Conditions

In case of an open-circuit fault affecting DCA1, the switching state "O" becomes impossible for a positive phase current. Indeed, under normal conditions, when the switching state "O" is activated, the positive phase current flows through $T12$ and DCA1 as shown in Fig. 3(a). However, under faulty condition of DCA1, the current path is established through D13 and D14. Thus, the output pole voltage becomes $(-VDC/2)$ instead of zero, leading to a significant modification of the CMV signature as shown in Fig. 2(b). One can observe a substantial increase of its dv/dt. This distortion will in turn affect the phase current quality. If an open-circuit fault occurs in DCA2, the negative

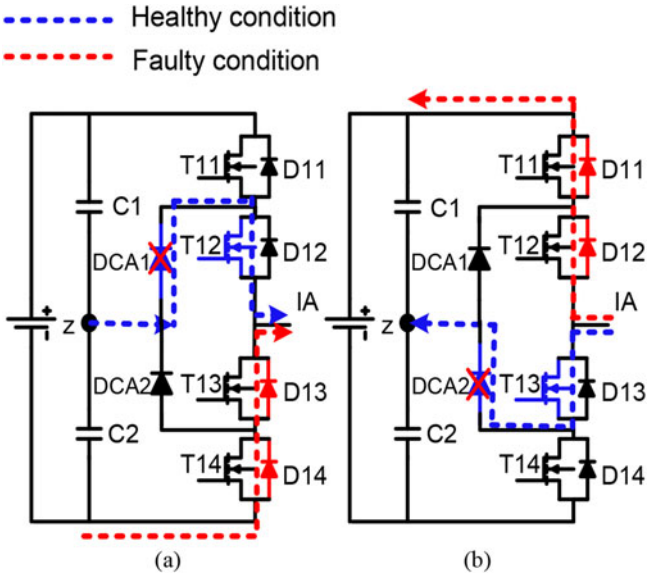

Fig. 3. Current paths for normal and open-circuit fault conditions of: (a) clamping diode DCA1 and (b) clamping diode DCA2.

current will inherently flow through D12 and D11, instead of DCA2 and *T*13. Fig. 3(b) shows the corresponding path of the negative current under both faulty and normal situations. Consequently, the pole voltage of the corresponding phase is changed to $+V\mathrm{DC}/2$ instead of zero which affects the CMV signature as illustrated in Fig. 2(c), where an important increase of its d*v*/d*t* is also observed. The latter situation also causes undesirable distortions in the phase current waveform.

C. Diodes Failure Effect on the Conducted Emissions

Basically, the commutation phenomenon of static power converters gives rise to common-mode emissions caused by the following two reasons.

1) The CMV defined in (1) is not constant because of the modulation principle [23]. The high-frequency variation of this voltage creates in turn a common-mode current ($i_{\mathrm{cm}g}$) that circulates from the inverter's ac terminals to the ground through the load and the parasitic capacitor c_{pg} as shown in Fig. 4. Since each clamping diode failure affects the waveform of CMV and increases its d*v*/d*t*, it consequently modifies the common-mode emissions signature.
2) High-frequency voltage oscillations are induced by the commutation process of the power switches, the leakage inductors found in the printed circuit board (PCB) board, and the parasitic capacitors. This phenomenon causes common-mode current $i_{\mathrm{cm}} = \sum_i i_{\mathrm{cm}\,i}$ flowing to the ground through the parasitic capacitors c_{pi} which link the heat sink to the power semiconductor devices. Moreover, it is well known that a diode drastically contributes to the generation of the electromagnetic interferences mainly because of the reverse recovery current associated to the carrier majority type of diodes [24]. Consequently, the absence of a clamping diode caused by an open-circuit fault has a direct impact on the signature of i_{cm}.

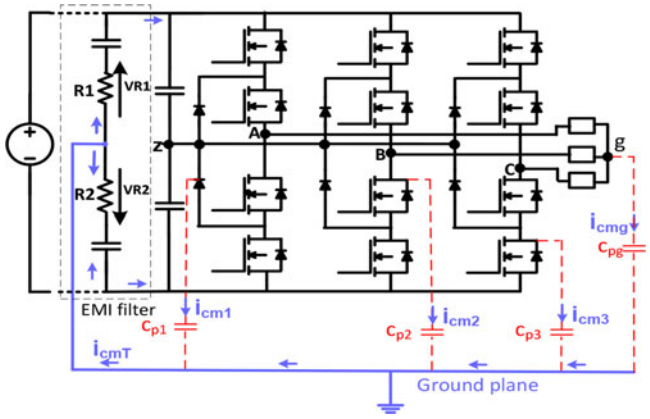

Fig. 4. Common-mode current-loop (C_{pi} are parasitic capacitors emulating the common-mode propagation paths to the ground of currents $i_{\mathrm{cm}\,i}$).

The total common-mode current as defined by (2) and shown in Fig. 4 follows the path to the dc voltage source through the ground plane. Using Kirchhoff's law, one can write the following equation:

$$i_{\mathrm{cm}T} = i_{\mathrm{cm}g} + \sum_i i_{\mathrm{cm}i}. \tag{2}$$

Since this current includes useful information about the state of health of the clamping diodes, an image of this current can be obtained by connecting an appropriate EMI filter between the dc source and the inverter's dc terminals. A true image of the conducted emissions is therefore collected by measuring *VR*1 and *VR*2 voltages across both resistors *R*1 and *R*2 of the EMI filter.

According to the analysis which was just introduced, a failed clamping diode can be identified by processing the conducted electromagnetic signature as will be investigated in the remaining part of this paper. Moreover, since the near-field emissions are assumed to be the image of the conducted emissions, the fault diagnosis based on the analysis of the near-field will also be investigated in this paper.

III. Numerical Simulations Using High-Frequency Model of the NPC Inverter

A. High-Frequency Modeling of Three-Level NPC Inverter

In order to emphasize the effectiveness of the previously presented theoretical analysis, showing the effect of clamping diodes failure on the signature of common-mode emissions, a high-frequency model of the NPC inverter feeding a three-phase RL load is first developed as shown in Fig. 5(a). Each transistor and its freewheeling diode are modeled using the spice three-level model of a MOSFET and two parasitic inductors for the source and the drain connection sides as depicted in Fig. 5(b). Each transistor gate is connected to a programmable voltage supply that emulates the gate signal provided by the controller.

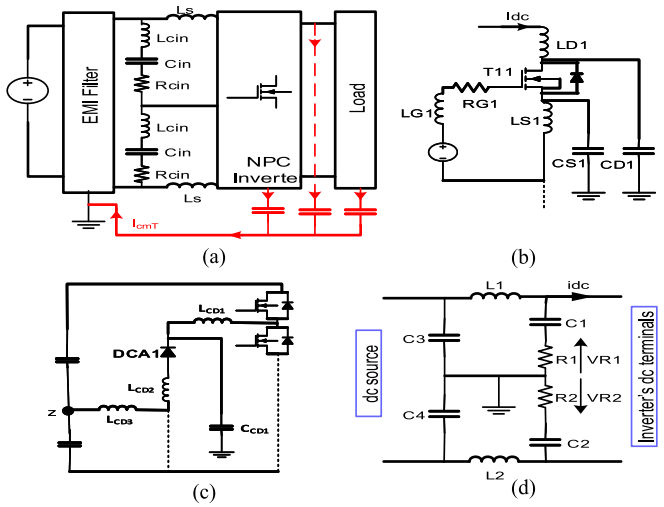

Fig. 5. High-frequency model of the three-level NPC inverter (a) general setup, (b) high-frequency components associated with a transistor and its freewheeling diode, (c) high-frequency components associated with a clamping diode, and (d) EMI filter.

TABLE I
SYSTEM PARAMETERS USED FOR THE HIGH-FREQUENCY MODELING

Symbol	Value	Symbol	Value
Cin	1000 μF	LS1	5 nH
$C1 = C2$	220 nF	RG1	8
$C3 = C4$	8 μF	LG1	5 nH
$CS1 = CD1$	130 pF	$Rcin$	0.2 Ω
$Lcin$	50 nH	$R1$	50 Ω
Ls	100 nH	$R2$	50 Ω
$L1$	50 μH	LCD1	6.6 nH
$L2$	50 μH	LCD2	17.27 nH
LD1	10 nH	LCD3	20 nH

This connection is modeled by a leakage inductor along with a resistor. The drain and source are coupled to the ground via parasitic capacitors of a few tens of pF. The presence of these capacitors is due to the virtual channels created between the power components and the ground plane through the heat sink. On the other hand, each clamping diode is represented by the spice model and three leakage inductors as shown in Fig. 5(c). The high-frequency coupling to the ground is modeled by a parasitic capacitor connected to the cathode. A standard EMI filter circuit model was chosen as shown in Fig. 5(d) [25]. The latter behaves as a low-pass filter that isolates the dc bus and dc source from the high-frequency conducted emissions. The latter are filtered to the ground through the two $C1$ and $C2$ capacitors. The $R1$ and $R2$ resistors are inserted in the path to the ground of the conducted emissions with the aim to measure the signature of these emissions. The system parameters used for the high-frequency modeling and for the numerical simulations are presented hereafter in Table I.

B. Numerical Simulations

Numerical simulations are performed using a time domain circuit simulator executing the numerical model at 100 ns time step. Fig. 6 illustrates the waveforms of the pole voltage V_{Az} and three load currents obtained with the following three different scenarios: normal steady-state healthy condition, open-circuit fault of DCA1, and open-circuit fault of DCA2. The obtained results are in good agreement with the theoretical analysis. Indeed, each clamping diode failure causes undesirable distortions in the load currents waveforms. Moreover, the failure of DCA1 affects the positive part of the pole voltage waveform, while the failure of DCA2 affects only the negative part of the same voltage waveform.

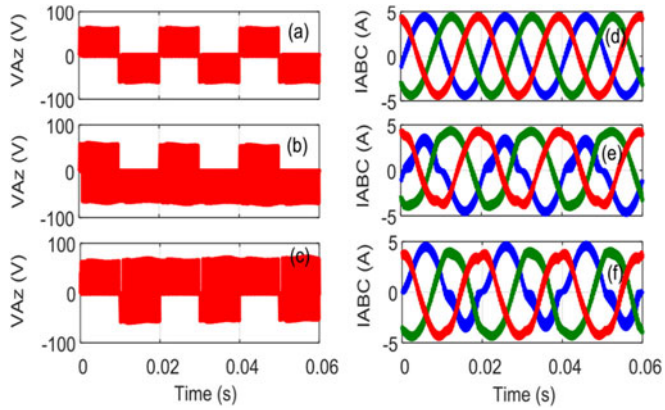

Fig. 6. Simulated pole voltage V_{Az} and load currents obtained with the following conditions (a)–(d) healthy operation, (b)–(e) DCA1 open-circuit fault, and (c)–(f) DCA2 open-circuit fault.

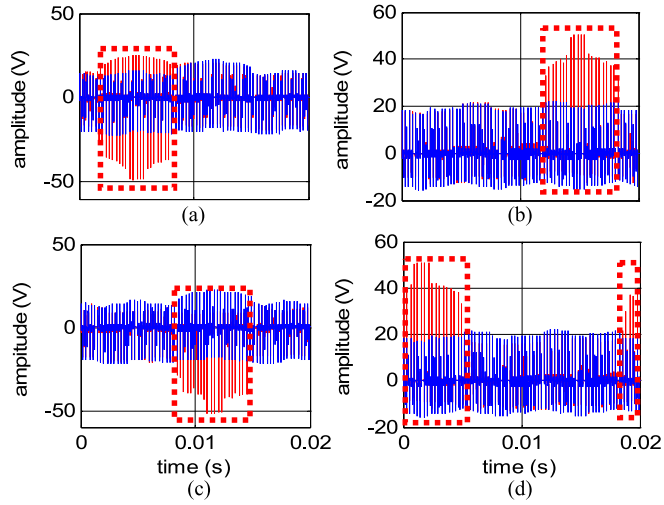

Fig. 7. Simulated voltage waveforms obtained across $R1$ EMI filter resistor with faulty clamping diode (red) and without faulty clamping diode (blue), (a) DCA1 fault, (b) DCA2 fault, (c) DCB1 fault, and (d) DCB2 fault.

Fig. 7 displays the waveform of the voltage $VR1$ measured across the EMI filter resistor $R1$ which is indeed an image of the conducted emissions. The simulation results are obtained with an affine sampling time equal to 10 ns. It is clear that the signature of the conducted emissions changes only in the region where the faulty diode is able to conduct. This signature pattern change which is visible to the bare eye is characterized by higher voltage peaks. It can therefore be considered as an informative signature of the faulty device. Further analysis of

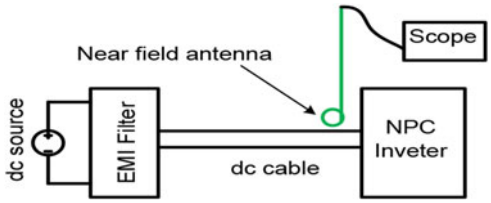

Fig. 8. Near-field antenna location above the dc-bus cable.

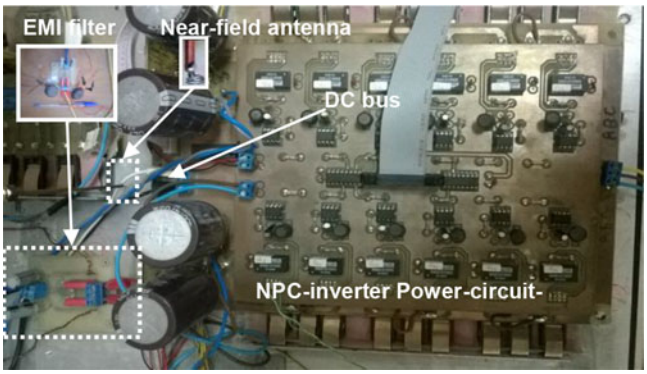

Fig. 9. Photograph showing the EMI filter and near field antenna positions with respect to the NPC inverter power circuit.

the EMI signature will be investigated in the following section based on experimental results.

IV. Analysis of Conducted Emissions Based on Experimental Results and Automatic Classification of the Fault

A. Description of the Experimental Setup

Experimental tests are carried out on a laboratory prototype of a three-phase three-level NPC inverter operating with and without faulty clamping diodes. The NPC inverter makes use of 12 MOSFET power transistors IRF740 and the 6 clamping diodes are of 15ETH06 type. The control signals are provided by the DSP TMS320F28335. The inverter operates with a switching frequency and modulation index equal to 3 kHz and 0.8, respectively. A simple and low-cost PCB is realized for the EMI filter that is used for the measurement of the conducted emissions fed back to the inverter's dc side. A near-field antenna is also placed above the inverter's dc-bus cable with the aim to collect the radiated emissions as shown in Fig. 8. The photograph in Fig. 9 illustrates the EMI filter and near-field antenna positions with respect to the NPC inverter power circuit. The analysis of the near-field emissions will be addressed in Section V. It is also noteworthy to underline that the use of near-field antenna allows avoiding any direct contact with the inverter circuit that may cause system parameters changes. This can be considered as an important benefit for the real-time diagnosis and monitoring of industrial electronic devices.

B. Analysis of Conducted Emissions

1) Single Clamping Diode Open-Circuit Fault: A first test is carried out under healthy operation condition. Six other tests are also carried out with an open-circuit fault affecting only one clamping diode. Fig. 10 illustrates the voltage waveforms across the EMI filter resistor $R1$. All measurements are synchronized with the gate signal first rising edge of transistor $T11$. The peaks value of the voltage under healthy conditions does not exceed 1 V. As for the DCA1 fault case, the peaks amplitude may reach 4–5 V. This substantial variation only occurs within the time interval [0, 10] ms, where the diode is supposed to commutate. Similar results are obtained in case of an open-circuit fault affecting the remaining clamping diodes. The obtained results confirm therefore that the voltage across $R1$ effectively includes a specific electromagnetic signature that appears during the appropriate switching interval of the faulty diode. This signature is characterized by a significant amplitude increase of the conducted emissions during the time interval where the diode is assumed to commutate. This phenomenon is mainly due to the increase in the dv/dt of the CMV as already explained in Section II-B. Consequently, the conducted emissions sustain a certain increase. Notice that the amplitude of the voltage peaks may change a bit according to the inverter's topology, PCB layout design, parasitic parameters, power electronic systems technology, operating conditions, load values, etc. Nevertheless, the variations in the amplitude of peaks are detected to identify the fault, rather than their absolute level. The region where the abnormal voltage peaks occurred is identified to point out the faulty component. Moreover, the identification time is equal to a half of the fundamental period, which corresponds to the appearance of the fault signature. On the other hand, unlike the diagnosis techniques based on the analysis of the pole voltages [15], this method does not require a prior knowledge of all power devices' switching states. Only, an image of $T11$ gate signal is used to identify the operation interval of each clamping diode.

2) Multiple Clamping Diode Open-Circuit Fault: Many experimental tests were carried out for different combination of double open-circuit faults. An example of the obtained results is illustrated in Fig. 11; the results depicted in top and middle positions are for the voltages waveforms as measured across the resistors $R1$ of EMI filter having an open-circuit fault of DCA1 and DCB2, respectively. The curve in the bottom position illustrates the voltage across $R1$ with a multiple fault affecting DCA1 and DCB2 simultaneously. The obtained results show clearly that electromagnetic signature of the two simultaneous clamping diodes open-circuit fault is equivalent to the superposition of DCA1 and DCB2 single fault signatures. In other words, a double open-circuit fault does not create common-mode emissions outside the operation intervals of the faulty diodes. This very important result confirms therefore that this method is valid for detection either single or double open-circuit faults.

C. Fault Classification

Though the conducted emissions signatures obtained with both the simulation and experimental tests are well visible, an automatic classification is necessary to perform a systematic distinction of each defective case. Given this fact, the time interval of each signature zone should be scrupulously delimited. In case

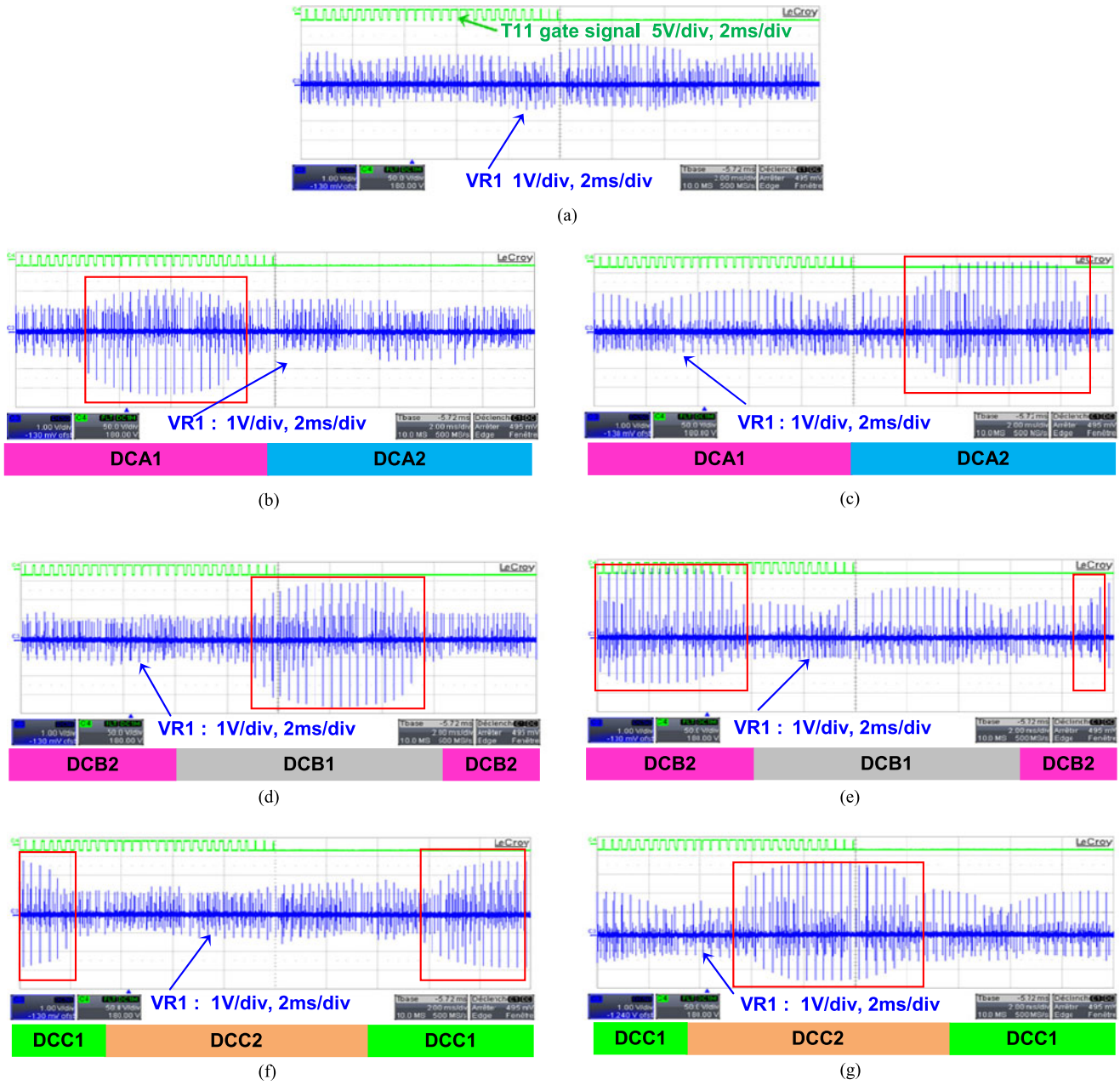

Fig. 10. Waveforms (blue) of voltage *VR*1 across the EMI filter in healthy and faulty operations (green) gate signal of *T*13 to show the synchronization of experimental measurements.

of DCA1 fault, the temporal location of the signature is centered in the first half-period (0 to 10 ms). More precisely, most significant peaks appear between 3.3 and 6.6 ms. Therefore, this interval will be associated with DCA1. Likewise, DCA2 signature peaks are expected to be well distinguished between 13.3 and 16.6 ms. The same interpretation is valid for the remaining diodes DCB1, DCB2, DCC1, and DCC2. Accordingly, the fundamental period is divided into six equal time intervals namely *T*1, *T*2 . . . *T*6. Fig. 12 shows the temporal locations of these six time intervals associated with their corresponding diodes. On the other hand, envelope detection is applied to voltage *VR*1 during each time interval *Ti* ($i = 1, \ldots, 6$) with the aim to follow the general trend of the brief high-frequency signature peaks. The fault diagnosis is therefore performed as follows: Each pattern's value of the envelope recorded during the actual time interval *Ti* ($i = 1, 2, \ldots, 6$) is subtracted from the one of the previous time interval *Ti*–1. The subtraction results are thereafter integrated along the entire time interval *Ti* ($i = 1, \ldots, 6$) using the trapezoidal discrete integration method. This technique will allow detecting the abrupt variation in the EMI signature with respect to the previous time interval. Indeed, integration with respect to time will provide high values when the HF peaks appear due to a faulty component. Fig. 13 shows the EMI signature (voltage *VR*1) and its envelope detection recorded in case of DCA1 fault. Certainly, the integral of the envelope subtraction between the samples of *T*2 and *T*1 will be greater than its value elsewhere

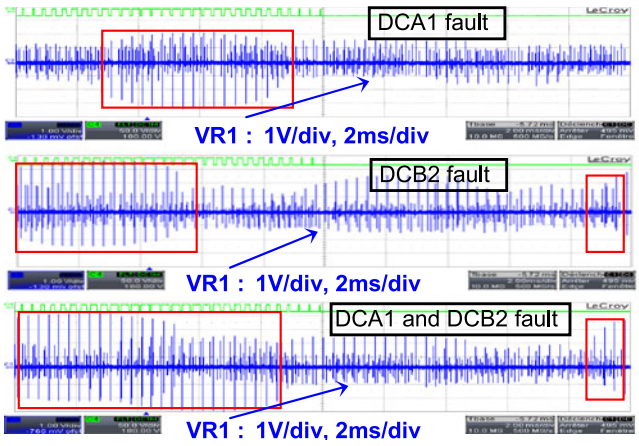

Fig. 11. Measured waveforms of voltage across the EMI filter resistors in case of DCA1 single fault, DCB2 single fault and DCA1–DCB2 double fault.

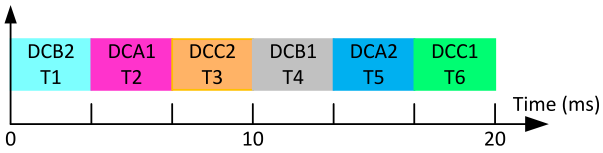

Fig. 12. Allocation of each faulty diode signature zone with its exact time interval Ti $(i = 1, \ldots, 6)$.

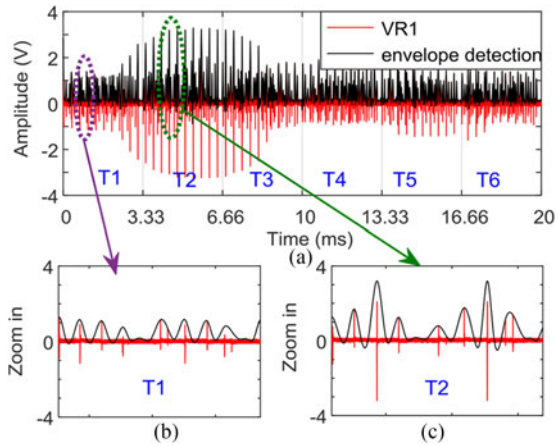

Fig. 13. (a) Envelope detection of the *VR*1 signal in case of open-circuit fault in DCA1, (b) zoom in within the interval *T*1, and (c) zoom in within the interval *T*2.

over the fundamental period. Moreover, a negative value of the envelope integration is expected in the next time interval *T*3 because of the fall of the HF peaks in comparison with *T*2.

Table II shows the obtained results after subtraction of each two adjacent envelopes and integration along an entire time interval Ti $(i = 1, \ldots, 6)$. The results are obtained in healthy case with $m = 0.8$, six possible single diode faults with $m = 0.8$, DCA1 fault with a low modulation index $(m = 0.4)$, and (DCA1, DCB2) faults. The highest integral value in each case is highlighted with blue color. The value in the next time interval is highlighted with yellow color. It is clear that when a diode is faulty, the value of the integral within its specific time interval

TABLE II
INTEGRATION RESULTS OF THE SUBTRACTED TWO ADJACENT ENVELOPES OVERT THE SIX TIME INTERVALS Ti $(i = 1, \ldots, 6)$ (RESULTS MULTIPLIED BY 10 000)

	T1	T2	T3	T4	T5	T6
Healthy	4.8878	-6.3692	2.7172	15.9471	-6.9997	-10.1831
DCA1	7.4068	74.3912	-36.4268	-19.6055	-21.0954	-4.6703
DCA2	-32.8926	-6.5104	14.2858	14.2858	56.8950	-46.2826
DCB1	1.7532	6.6171	3.7402	94.9851	-62.4684	-44.6273
DCB2	73.9581	-41.6067	22.5036	7.9353	-3.8837	-13.8994
DCC1	-34.1634	-32.5711	6.7991	27.5691	-15.3233	47.6895
DCC2	17.3993	-18.1563	85.4174	-32.4049	-39.8197	-12.4357
DCA1 for m=0.4	-12.5897	65.4107	-49.0507	-2.1425	14.4488	-16.0766
DCA1 and DCB2	65.6250	11.4232	-29.5205	38.3587	-15.6584	6.4893

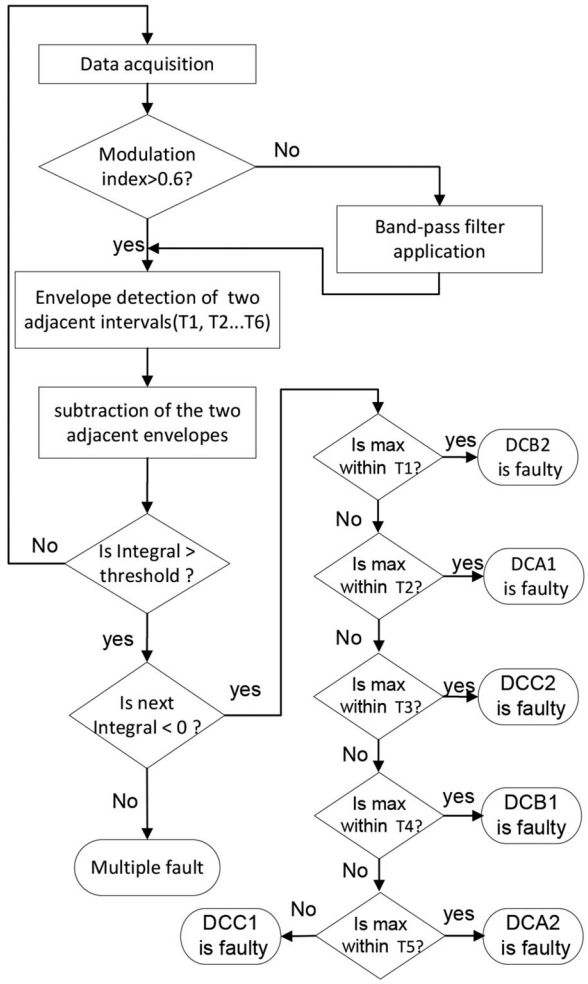

Fig. 14. Flowchart of the fault detection algorithm.

is greater than the remaining other cases. Therefore, a clamping diode fault is declared whenever an integral value is greater than a threshold value (in this case, the threshold is fixed to 40). Moreover, if the integral value corresponding to the next time interval $Ti + 1$ is negative, this means that the diode associated with this interval is safe. This scenario corresponds therefore to a single diode fault. Otherwise, a positive value of the integral

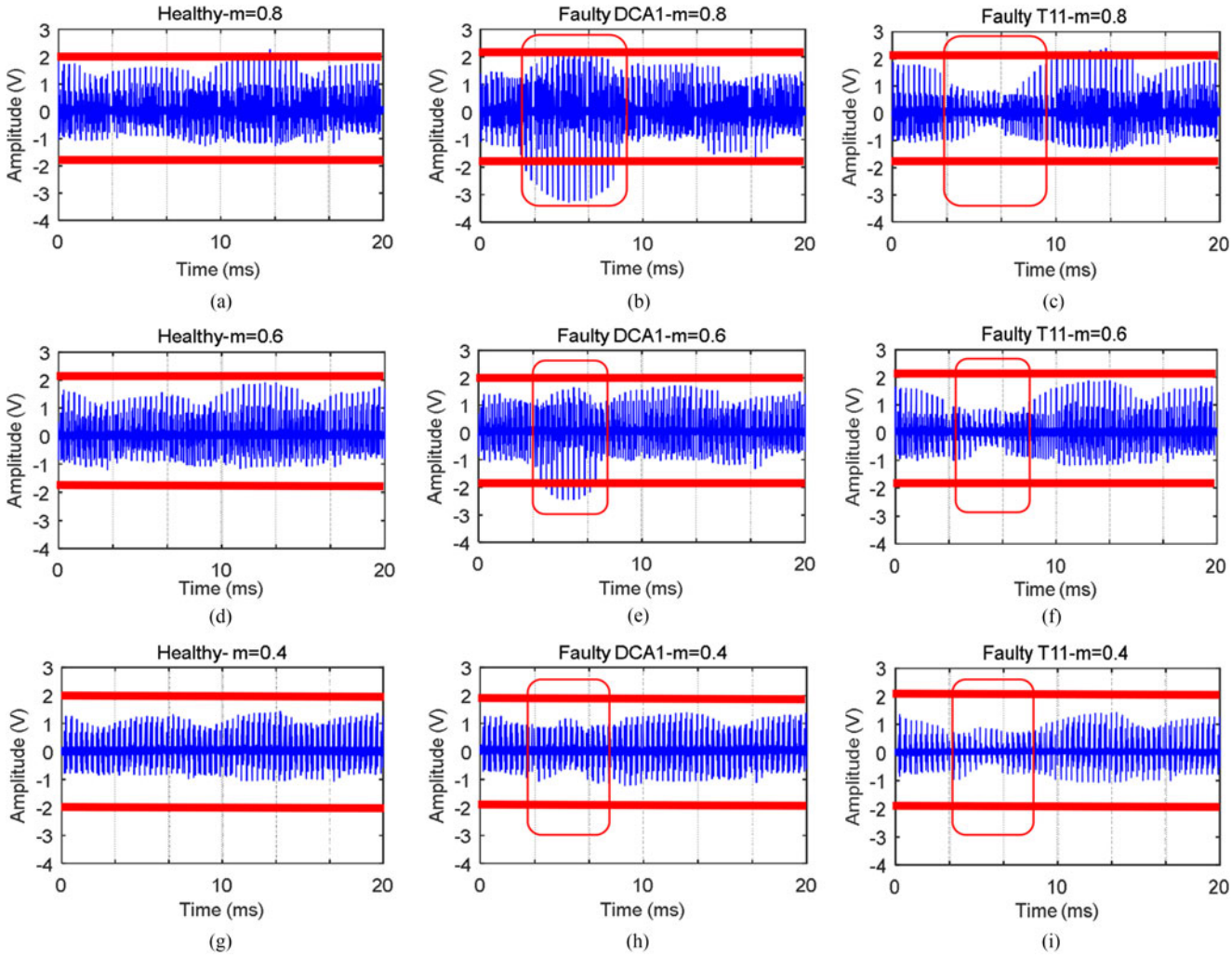

Fig. 15. Voltage *VR*1 obtained with three values of the modulation index ($m = 0.4$, 0.6, 0.8) and three operation scenarios (a)–(d)–(g) healthy case, (b)–(e)–(h) DCA1 open-circuit fault DCA1, and (c)–(f)–(i) *T*11open-circuit fault.

in the next interval implies that the diode associated with this interval $Ti + 1$ is also faulty. Therefore, a multiple diodes fault is declared. The flowchart of Fig. 14 summarizes the whole fault detection algorithm. This algorithm can easily be applied online by simply choosing the threshold value and controlling the integral's sign in the next interval. In addition, this classification method does not require extra memory to store the healthy case data. Thus, it is very useful for the diagnosis process.

D. Evaluation of Similarity With Active Switch Signature

To evaluate the signature similarity caused by *T*11 and DCA1 open-circuit faults, several experimental tests are carried out with the following three scenarios: healthy case, DCA1 fault, and *T*11 fault. Fig. 15 hereafter illustrates the experimental waveforms obtained with three values of the modulation index: $m = 0.8$, $m = 0.6$, and $m = 0.4$. For $m = 0.6$, and $m = 0.8$, the open-circuit faults in DCA1 and *T*11 provide different easily distinguishable electromagnetic signatures as can be seen in Fig. 15. Indeed, the DCA1 fault increases voltages peaks amplitude in *VR*1 during the first half-period [0, 10] ms as compared

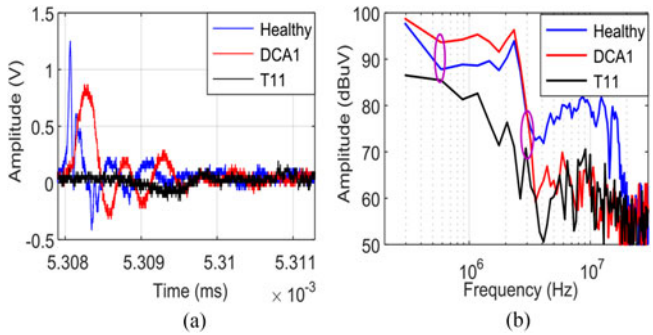

Fig. 16. (a) Zoom in of the voltage across resistor *R*1 within the signature area and (b) frequency spectrum within the zoom window.

to the healthy case. However, the *T*11 fault leads to a remarkable decrease in the amplitude of the voltage peaks during the same time interval.

For $m = 0.4$, it has become difficult to observe as well as to detect the difference between the faulty cases of DCA1 and *T*11 without additional post processing of the obtained signatures. To overcome this limitation, the fast Fourier transform (FFT)

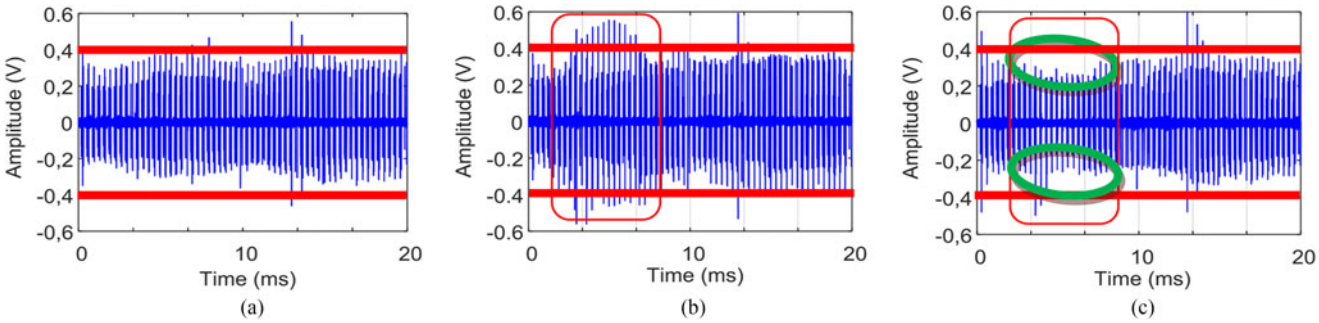

Fig. 17. *VR*1 obtained with $m = 0.4$ and filtered with an order 20 bandpass filter (a) healthy case, (b) DCA1 fault, and (c) *T*11 fault.

is applied to several samples of *VR*1 within the signature area. The time window of FFT is set to 3.3 μs. Fig. 16(a) shows an example of *VR*1 waveform within these specific windows for the three operation cases (Healthy, DCA1 fault, and *T*11 fault). The obtained frequency spectra are illustrated in Fig. 16(b). It is clear that the DCA1 fault causes a substantial increase in the spectral rails amplitude for frequency range [0.5, 3] MHz, compared to the *T*11 fault case. According to this frequency analysis, it is judicious to apply a bandpass filter to the fault signature for low values of the modulation index. Fig. 17 displays the voltage *VR*1 filtered with an order 20 bandpass filter for the three operation cases (healthy, DCA1 fault, and *T*11 fault). The filter bandwidth is set to [0.5, 3] MHz in order to be consistent with the results obtained with the FFT analysis. The obtained results show clearly the difference between the collected filtered signatures of DCA1 and *T*11. Indeed, the DCA1 fault increases the amplitude of voltage peaks in the filtered waveform of *VR*1, while the *T*11 fault causes a decrease in peaks amplitude.

These results confirm the robustness of this method regardless of the modulation index value. Indeed, for high values of the modulation index, it is confirmed that the signatures of faults caused by DCA1 and *T*11 are quite different. As for low values of the modulation index, both signatures can be distinguished from each other by applying simply a bandpass filter to *VR*1.

E. Fault Detection Under Transient Working Conditions

To testify the robustness of the proposed fault detection method under transient working conditions, an additional experimental test was carried out where the modulation index is abruptly changed from $m = 0.6$ to $m = 0.8$ [see Fig. 18(c)]. Two other tests were carried out in steady-state operation with $m = 0.8$ and $m = 0.6$ [see Fig. 18(a) and (b)]. The comparison of voltage *VR*1 waveforms obtained during transient and steady-state operation showed that EMI signature remains almost unchanged despite the variation of the modulation index. To confirm this observation, an automatic classification is performed using the same method already explained in detail in Section IV-C. The obtained results are given in Table III. The values of integrals computed within diode DCA1 operation time interval *T*2 are almost the same and superior to the threshold value during the steady-state and transient operations of the converter. This confirms that the DCA1 fault can also

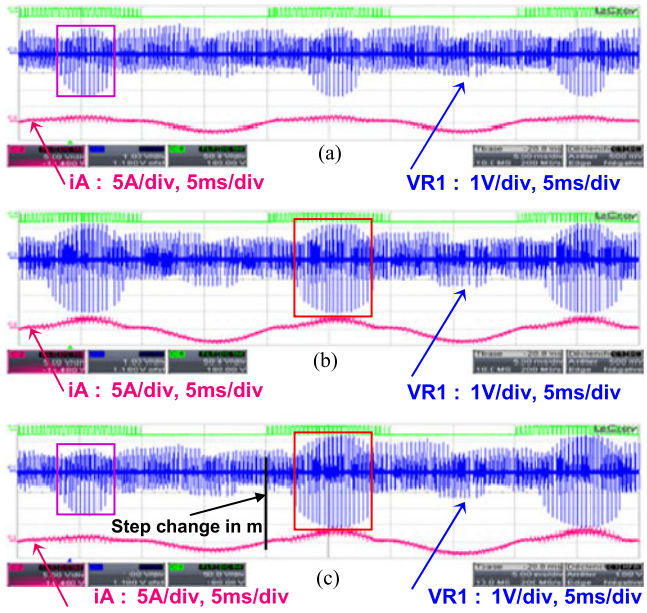

Fig. 18. Measured waveforms of voltage *VR*1 across the EMI filter resistor and load current iA obtained with: (a) DCA1 fault in steady state operation with $m = 0.6$, (b) DCA1 fault in steady-state operation with $m = 0.8$, and (c) DCA1 fault during a step increase in *m* from 0.6 to 0.8.

TABLE III
AUTOMATIC CLASSIFICATION UNDER TRANSIENT AND STEADY-STATE OPERATION WITH DCA1 FAULTY CLAMPING DIODE (RESULTS MULTIPLIED BY 10 000)

		T1	T2	T3	T4	T5	T6
Steady state/m=0.6		0.223	107.616	-83.594	2.133	-18.96	-3.151
Steady state/m=0.8		5.605	230.747	-157.667	30.452	-19.925	-28.306
Transient state	m=0.6	-0.297	108.991	-102.4	18.593	-18.757	-6.128
	m=0.8	-4.064	233.026	-149.59	19.786	-35.508	-24.077

be detected during transient operation. Moreover, the integral's values calculated within the next time interval *T*3 remain also negative during the transient operation. This implies that the fault is effectively single. It can therefore be concluded that this method is effective in detecting the appropriate faulty clamping diode in case of transient operation of the converter.

V. Analysis of Radiated Emissions Based on Experimental Results

Since the emitted near-field (radiated interferences) represents the image of the conducted emissions, a magnetic probe (antenna) is therefore used to capture the near-field in order to prevent any electrical connection with the inverter. The captured flux variations induce an electromotive force across the near-field probe according to the Lenz–Faraday law. The voltage $V(t)$ across the probe can be expressed as follows:

$$V(t) = \oint -\frac{\partial B}{\partial t}\, dS. \tag{3}$$

Since the probe surface S is very small as compared to the length of the near-field waves, therefore the magnetic induction can be considered constant along the probe surface. Consequently, the maximum amplitude of the induced voltage V at a specific frequency f_S of the magnetic near-field is deduced from (3) as follows:

$$V(f_s) = 2\,\pi\, f_s\; B\; S. \tag{4}$$

B and f_S are the amplitude and frequency of the magnetic induction. By replacing in (4) the magnetic induction B by $\mu_0 . H$, one can deduce that the amplitude of the near-field H at a specific frequency is equivalent to the electromotive force induced by the probe as given by the following equation hereafter, where $\mu_0 = 4\pi 10^{-7}$ is the vacuum permeability:

$$H(f) = V(f)/2\pi\,\mu_0\, f_s\; S. \tag{5}$$

For this purpose, the measured voltage across the near-field probe is first saved in the scope memory as a data file and exported to a signal processing software. Thereafter, the FFT is applied to several samples inside and outside the signature area of each clamping diode. The time window of the FFT is set to 3.3 μs.

Fig. 19(a) shows the waveforms of the near-field probe voltage measured in the time-domain obtained with healthy operation and DCA1 open-circuit fault. Unlike the former case of conducted emissions, the variation in the emitted near-field amplitude is not distinguishable with the bare eye. For this purpose, two zooms in of the emitted near-field are performed. The first one is done outside the signature area of DCA1 and displayed in the top of Fig. 19(b). The results show that the amplitude and oscillating cycle remain unchanged. The latter oscillating period is kept near 26 ns for both cases. The frequency spectra shown in the bottom part of Fig. 19(b) emphasize this ascertainment, where the most important spectral rail remains located at 40 MHz for the healthy and faulty cases.

A second zoom in is performed within the signature area of DCA1 and illustrated in the top part of Fig. 19(c). The obtained result shows a substantial decrease in the radiated emission frequency, where the fundamental period is changed from 26 (healthy case) to 290 ns (faulty case). This observation is confirmed by inspecting the frequency spectra displayed in Fig. 19(c) (bottom part). We can clearly observe that the open-circuit fault of DCA1 causes a substantial decrease in the spectral rail amplitude located at 40 MHz, while giving rise to a new spectral rail located at 3.4 MHz. This information extracted

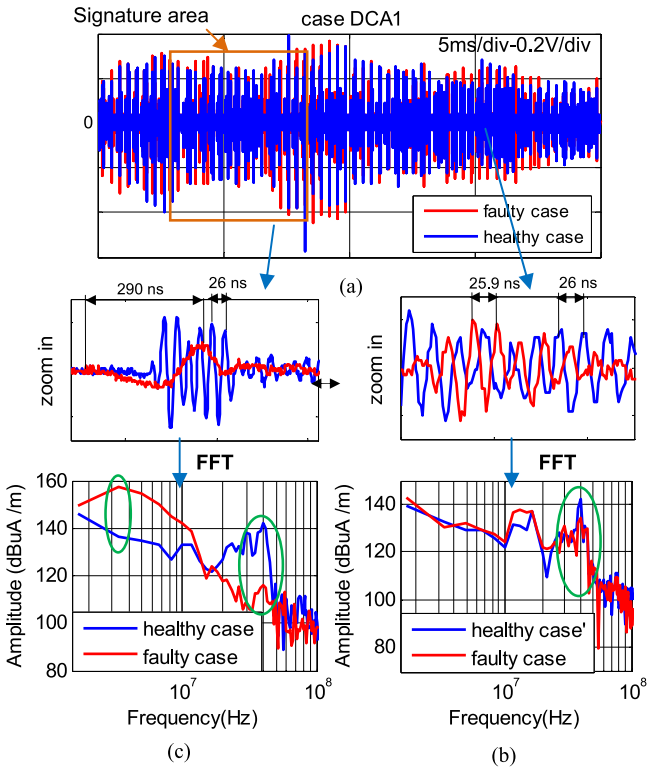

Fig. 19. (a) Voltage across the near-field probe in healthy condition (blue) and with DCA1 clamping-diode open-circuit fault (red), (b) zoom in of the window outside the signature area and its corresponding near-field spectrum, and (c) zoom in of the window inside the signature area and its corresponding near-filed spectrum.

from the high-frequency emission within the signature area of DCA1 is therefore very useful to detect the open-circuit fault of DCA1.

It is worth noting that some specificities should be respected with the aim to reduce the impact of the ambient EMI on the accuracy of the proposed method: First, the location and the diameter of the antenna have a significant impact on the near-field measurement. Therefore, the antenna loop should be small and close enough to the converter [26]. The loop diameter utilized in this paper is very small (only 3 mm). The probe is placed close to the inverter (10 mm above the dc-bus connector). Second, the impact of ambient EMI can be further mitigated by applying a bandpass filter to the voltage across the near-field probe. This filter bandwidth needs to be designed so as to preserve the spectral rails that are located at the most informative frequency and to exclude the unwanted components such those found in the ambient EMI. A more robust solution against ambient EMI uses a noise cancellation algorithm involving, for example, a Weiner filter [27]. Note even when a disturbing noise is intentionally produced in order to alter the detection system, it should be applied exactly at the time/frequency location of the fault, and should have the same amplitude of the fault signature. Only under these specific conditions, a false alarm may be generated. Hence, it is almost impossible to disturb the obtained signatures if the aforementioned conditions are completely satisfied.

VI. Conclusion

This paper presented two nonintrusive detection methods of open-circuit faults affecting the clamping diodes of the three-level NPC inverter topology used for medium power applications. The first one was based on the analysis of the common mode emissions signature in the dc bus by sensing the voltage across a simple and low-cost EMI filter. It was shown that a clamping diode failure leads to a substantial increase in the conducted emissions amplitude in the specific time interval, where the faulty diode is assumed to commutate. This first technique is also effective when it comes to detect a multiple open-circuit fault, which constitutes a very important benefit. A classification method was also proposed with the aim to perform an automatic fault detection. The second technique was based on the frequency domain analysis of the near-field emitted by the dc bus. An FFT of the probe voltages performed for each window enclosing the time interval where one of the six diodes is able to commutate. The obtained results showed an open-circuit diode fault leads to a substantial decrease in spectrum amplitude at a specific radio frequency and the appearance of new spectral rail. This second technique does not require extra hardware connection or modification on the inverter power circuit, which makes it a fault diagnosis wireless promising technique for the already existing industrial power electronics NPC inverters. In view of expanding the proposed technique to diagnose complex structures involving great number of power devices, such as MMC, the authors propose placing an EMI filter on the dc bus of each isolated dc source. This will make the localization of the faulty cell easier, since its electromagnetic signature is found in the measured voltage of corresponding EMI filter.

References

[1] K. K. Gupta, A. Ranjan, P. Bhatnagar, L. K. Sahu, and S. Jain, "Multilevel inverter topologies with reduced device count: A review," *IEEE Trans. Power Electron.*, vol. 31, no. 1, pp. 135–151, Jan. 2016.

[2] J. I. Metri, H. Vahedi, H. Y. Kanaan, and K. Al-Haddad, "Real-time implementation of model-predictive control on seven-level packed U-cell inverter," *IEEE Trans. Ind. Electron.* vol. 63, no. 7, pp. 4180–4186, Jul. 2016.

[3] J. Lamb and B. Mirafzal, "Open-Circuit IGBT fault detection and location isolation for cascaded multilevel converters," *IEEE Trans. Ind. Electron.*, vol. 64, no. 6, pp. 4846–4856, Jun. 2017.

[4] F. Blaabjerg, M. Liserre, and K. Ma, "Power electronics converters for wind turbine systems," *IEEE Trans. Ind. Appl.*, vol. 48, no. 2, pp. 708–719, Mar./Apr. 2012.

[5] S. Yang, A. Bryant, P. Mawby, D. Xiang, L. Ran, and P. Tavner, "An industry-based survey of reliability in power electronic converters," *IEEE Trans. Ind. Appl.*, vol. 47, no. 3, pp. 1441–1451, May/Jun. 2011.

[6] T. Wang, H. Xu, J. Han, E. Elbouchikhi, and M. E. H. Benbouzid, "Cascaded H-bridge multilevel inverter system fault diagnosis using a PCA and multiclass relevance vector machine approach," *IEEE Trans. Power Electron.*, vol. 30, no. 12, pp. 7006–7018, Dec. 2015.

[7] J. H. Choi, S. Kim, D. S. Yoo, and K. H. Kim, "A diagnostic method of simultaneous open-switch faults in inverter-fed linear induction motor drive for reliability enhancement," *IEEE Trans. Ind. Electron.*, vol. 62, no. 7, pp. 4065–4077, Jul. 2015.

[8] J. S. Lee, K. B. Lee, and F. Blaabjerg, "Open-switch fault detection method of a back-to-back converter using NPC topology for wind turbine systems," *IEEE Trans. Ind. Appl.*, vol. 51, no. 1, pp. 325–335, Jan./Feb. 2015.

[9] C. Ui-Min, J. Hae-Gwang, L. Kyo-Beum, and F. Blaabjerg, "Method for detecting an open-switch fault in a grid-connected NPC inverter system," *IEEE Trans. Power Electron.* vol. 27, no. 6, pp. 2726–2739, Jun. 2012.

[10] A. M. S. Mendes, M. B. Abadi, and S. M. A. Cruz, "Fault diagnostic algorithm for three-level neutral point clamped AC motor drives, based on the average current Park's vector," *IET Power Electron.* vol. 7, no. 5, pp. 1127–1137, May 2014.

[11] L. June-Seok, L. Kyo-Beum, and F. Blaabjerg, "Open-Switch fault detection method of a Back-to-Back converter using NPC topology for wind turbine systems," *IEEE Trans. Ind. Appl.* vol. 51, no. 1, pp. 325–335, Jan./Feb. 2015.

[12] S. Farnesi, P. Fazio, and M. Marchesoni, "A new fault tolerant NPC converter system for high power induction motor drives," in *Proc. IEEE Int. Symp. Diagnostics Elect. Mach. Power Electron. Drives*, Sep. 2011, pp. 337–343.

[13] B. Lu and S. K. Sharma, "A literature review of IGBT fault diagnostic and protection methods for power inverters," *IEEE Trans. Ind. Appl.*, vol. 45, no. 5, pp. 1770–1777, Sep./Oct. 2009.

[14] T. J. Kim, W. C. Lee, and D. S. Hyun, "Detection method for Open-Circuit fault in Neutral-Point-Clamped inverter systems," *IEEE Trans. Ind. Electron.* vol. 56, no. 7, pp. 2754–2763, Jul. 2009.

[15] M. B. Abadi, A. M. S. Mendes, and S. M. Â. Cruz, "Method to diagnose open-circuit faults in active power switches and clamp-diodes of three-level neutral-point clamped inverters," *IET Elect. Power Appl.*, vol. 10, no. 7, pp. 623–632, Aug. 2016.

[16] U. M. Choi, J. S. Lee, F. Blaabjerg, and K. B. Lee, "Open-circuit fault diagnosis and fault-tolerant control for a grid-connected NPC inverter," *IEEE Trans. Power Electron.*, vol. 31, no. 10, pp. 7234–7247, Oct. 2016.

[17] T. Wang, J. Qi, H. Xu, Y. Wang, L. Liu, and D. Gao, "Fault diagnosis method based on FFT-RPCA-SVM for cascaded-multilevel inverter," *ISA Trans.*, vol. 60, pp. 156–163, Jan. 2016.

[18] P. Lezana, R. Aguilera, and J. Rodriguez, "Fault detection on multicell converter based on output voltage frequency analysis," *IEEE Trans. Ind. Electron.*, vol. 56, no. 6, pp. 2275–2283, Jun. 2009.

[19] B. Li, S. Shi, B. Wang, G. Wang, W. Wang, and D. Xu, "Fault diagnosis and tolerant control of single IGBT open-circuit failure in modular multilevel converters," *IEEE Trans. Power Electron.*, vol. 31, no. 4, pp. 3165–3176, Apr. 2016.

[20] M. Barzegaran, A. Mohamed, T. Youssef, and O. A. Mohammed, "Electromagnetic signature study of a power converter connected to an electric motor drive," *IEEE Trans. Magn.*, vol. 50, no. 2, pp. 201–204, Feb. 2014.

[21] Y. Chen, X. Pei, S. Nie, and Y. Kang, "Monitoring and diagnosis for the DC–DC converter using the magnetic near field waveform," *IEEE Trans. Ind. Electron.*, vol. 58, no. 5, pp. 1634–1647, May 2011.

[22] U. M. Choi, F. Blaabjerg, and K. B. Lee, "Reliability improvement of a T-type Three-Level inverter with Fault-Tolerant control strategy," *IEEE Trans. Power Electron.*, vol. 30, no. 5, pp. 2660–2673, May 2015.

[23] C. Jettanasen, F. Costa, and C. Vollaire, "Common-Mode emissions measurements and simulation in Variable-Speed drive systems," *IEEE Trans. Power Electron.*, vol. 24, no. 11, pp. 2456–2464, Nov. 2009.

[24] A. Hatanaka and T. Kawashima, "A recovery-diode model for analyzing EMC of an on-board power supply," in *Proc. 15th Eur. Conf. Power Electron. Appl.*, Sep. 2013, pp. 1–5.

[25] E. Rondon-Pinilla, F. Morel, C. Vollaire, and J. L. Schanen, "Modeling of a buck converter with a SiC JFET to predict EMC conducted emissions," *IEEE Trans. Power Electron.*, vol. 29, no. 5, pp. 2246–2260, May 2014.

[26] Z. Li, F. Tavernier, A. Brard, L. Krhenbhl, D. Voyer, and C. A. F. Sartori, "Error analysis for near-field emc problems based on multipolar expansion approach," *IEEE Trans. Magn.*, vol. 53, no. 6, Jun. 2017, Art. no. 8001304.

[27] C. Osterwise, S. L. Grant, and D. Beetner, "Reduction of noise in near-field measurements," in *Proc. IEEE Int. Symp. Electromagn. Compat.*, Jul. 2010, pp. 171–176.

Ibtissem Abari was born in Sousse, Tunisia, in 1989. She received the B.S. and M.S. degrees in electrical engineering from the National Engineering School of Sousse, University of Sousse, Sousse, Tunisia, in 2014 and 2015, respectively, where she is currently working toward the Ph.D. degree in electrical engineering.

She is a Member of the Laboratory of Advanced Technology and Intelligent Systems, National Engineering School of Sousse, University of Sousse. Her research interests include focused on multilevel inverters, reliability of power converters, and electromagnetic interferences.

Ali Lahouar was born in Sousse, Tunisia, in 1988. He received the B.S. degree in industrial electronics from the National Engineering School of Sousse, Sousse, in 2011, and the Ph.D. degree in electrical engineering from the National Engineering School of Tunis, Tunis, Tunisia, in 2016.

Since 2013, he has been a Researcher and Teacher with the University of Sousse, Sousse, and a member of the Laboratory of Advanced Technology and Intelligent Systems. His research interests include smart grids, renewable energy, electrical load/price forecast, wind/PV power prediction, and fault diagnosis of power converters.

Mahmoud Hamouda (M'15) received the B.S., Agregation, M.S., and Ph.D. degrees from ENSET and the Ecole Superieure des Sciences et Techniques, University of Tunis, Tunis, Tunisia, in 1995, 1996, 2004, and 2010, respectively, all in electrical engineering, and the HDR degree in electrical engineering from the University of Sousse, Sousse, Tunisia, in 2017.

He is currently an Associate Professor of electrical engineering with ISSAT, University of Sousse. He is affiliated with Canada Research Chair in Electric Energy Conversion and Power Electronics, Ecole de Technologie Supérieure, Montreal, QC, Canada. He is also a member of the Research Laboratory LATIS, National Engineering School of Sousse, University of Sousse. His main research interests include renewable energy conversion systems, digital signal processor, and field-programmable gate array for embedded real-time control, grid-connected converters, and fault diagnosis of power converters.

Jaleleddine Ben Hadj Slama (M'09–SM'13) was born in Akouda, Tunisia, on May 30, 1971. He received the engineer and Ph.D. degrees in electrical engineering from Ecole Centrale de Lyon, Lyon, France, in 1994 and 1997, respectively.

Since 2015, he has been a Full Professor of electrical engineering at the National Engineering School of Sousse, Sousse, Tunisia, where he is the leader of the EMC research group in the LATIS laboratory. His main research interests include electromagnetic compatibility of transportation systems, near-field techniques, EMI issues of power electronics systems and their modeling, smart grid, renewable energy and development of remote laboratories for Internet-Based Engineering Education.

Kamal Al-Haddad (S'82–M'88–SM'92–F'07) received the B.Sc.A. and M.Sc.A. degrees in electrical engineering from the University of Québec à Trois-Rivières, Trois-Rivières, QC, Canada, in 1982 and 1984, respectively, and the Ph.D. degree in electrical engineering from the Institut National Polytechnique, Toulouse, France, in 1988.

Since June 1990, he has been a Professor at the École de Technologie Supérieure, Montreal, QC, where he has been the holder of the senior Canada Research Chair in Electric Energy Conversion and Power Electronics since 2002. He has supervised more than 150 Ph.D. and M.Sc.A. students and coauthored more than 600 papers and 2 books. His research interests include high-efficiency power electronic converters, active and hybrid filters, modular multilevel converter, multilevel converters, and active rectifiers, including modeling, control, and development of industrial prototypes.

Dr. Al-Haddad is the 2016–2017 President of the IEEE Industrial Electronics Society and a Fellow of the Canadian Academy of Engineering.